Journal of Materials Chemistry A

Defect characterisation in Cu2ZnSnSe4 kesterites via resonant Raman spectroscopy and impact onto optoelectronic solar cells properties

Journal:	*Journal of Materials Chemistry A*
Manuscript ID	TA-ART-04-2019-003625.R1
Article Type:	Paper
Date Submitted by the Author:	23-Apr-2019
Complete List of Authors:	Dimitrievska, Mirjana; National Renewable Energy Laboratory; National Institute of Standards and Technology, NCNR; Catalonia Institute for Energy Research Oliva, Florian; Catalonia Institute for Energy Research Guc, Maxim; Catalonia Institute for Energy Research Giraldo, Sergio; Catalonia Institute for Energy Research Saucedo, Edgardo; Catalonia Institute for Energy Research Perez-Rodriguez, Alejandro; Catalonia Institute for Energy Research Izquierdo-Roca, Victor; Catalonia Institute for Energy Research

Defect characterisation in $Cu_2ZnSnSe_4$ kesterites via resonant Raman spectroscopy and impact onto optoelectronic solar cells properties

Mirjana Dimitrievska*[1,2,3], Florian Oliva[1], Maxim Guc[1], Sergio Giraldo[1], Edgardo Saucedo[1], Alejandro Pérez-Rodríguez[1,5], Victor Izquierdo-Roca*[1]

1 – Catalonia Institute for Energy Research (IREC), Jardins de les Dones de Negre 1, 08930 Sant Adrià de Besòs, Spain

2 – NIST Center for Neutron Research, National Institute of Standards and Technology, Gaithersburg, MD 20899-6102, United States

3 – National Renewable Energy Laboratory, Golden, CO 80401, United States

4 – Centres Científics i Tecnològics de la Universitat de Barcelona (CCiTUB), Lluís Solé i Sabarís 1-3, 08028 Barcelona, Spain

5 – IN^2UB, Departament d'Enginyeria Electrònica i Biomèdica, Universitat de Barcelona, C. Martí i Franquès 1, 08028 Barcelona, Spain

* Authors to whom correspondence should be addressed. E-mail: mirjana.dimitrievska@nist.gov, mirjana.dimitrievska@nrel.gov (M. Dimitrievska), vizquierdo@irec.cat (Victor Izquierdo)

Abstract:

Polycrystalline kesterite $Cu_2ZnSnSe_4$ (CZTSe) semiconductors have drawn attention as promising absorber candidates for the next generation of thin film photovoltaics. However, the narrow tolerance to stoichiometry variations that favours the formation of secondary phases and cluster defects is a challenging drawback that restrains the device performances. In this context Raman spectroscopy has demonstrated to be a powerful tool for the characterization of CZTSe, allowing the assessment of the relevant parameters such as structure, crystal quality and secondary phases.

In this work, multiwavelength Raman scattering measurements using nine excitation wavelengths (from 325 to 1064 nm) were performed on CZTSe polycrystalline thin films in order to give a detailed identification of all the active Raman modes expected in this crystalline structure. The experimental results compare well with the vibrational properties that have been computed by first-principles calculations based on density functional theory. Calculations of the phonon density of states (PDOS), as well as the simulation of the Raman spectra, have allowed a better understanding of the experimentally observed vibrational modes.

A "non-band gap resonant" Raman effect was observed under 325 nm excitation condition, making the ultra-violet (UV) Raman spectroscopy a very promising characterization technique due to its high sensitivity of the surface region which provides information of the buffer/absorber interface. Strong intensity enhancement of spectral regions around 176 cm^{-1} and 250 cm^{-1} is observed. Calculated PDOS and combinatorial experiments on more than 200 samples with stoichiometries close to the high efficiency device compositions, lead to the correlation of these intensities with the concentration

of V_{Cu} and Zn_{Sn} point defects, respectively. Correlation with the optoelectronic properties of the devices, allowed identification of the optimal concentration of V_{Cu} and Zn_{Sn} point defects for the highest performance devices. The application of the presented methodology has been confirmed by performing the same Raman analysis on the CZTSe absorber with 11% device efficiency. This work demonstrates that defect engineering in CZTSe is of the foremost importance for the improvement in the solar cell performance, and that UV-based Raman spectroscopy is an effective technique for the non-destructive assessment of defects in the kesterite materials.

Introduction

Polycrystalline kesterite $Cu_2ZnSnSe_4$ (CZTSe) and Cu_2ZnSnS_4 (CZTS) semiconductors, and their solid solutions $Cu_2ZnSn(S,Se)_4$ (CZTSSe) have drawn attention as promising absorber candidates for the next generation of thin film photovoltaics, with certified solar conversion efficiencies above 12% (13.8% small area device reported in late 2016).[1–6] The attractive properties of these materials include being constituted of only earth-abundant and non-toxic elements, as well as high tunability of their optical band gap in the range relevant for single-junction solar cell applications.[7,8] However, even with all these benefits, the efficiencies for this technology fell far below the 28% predicted from the Shockley−Queisser limit.[9,10] In order to reach the goal of >20% efficiency needed for the large-scale utilization of these materials, a better understanding of their limiting factors is needed.

A particular issue, that is very poorly understood, is the relationship between the composition of the kesterite phase and the resulting optoelectronic properties of the solar cell. Additional complicating matter in this case is also the use of off-stoichiometry conditions for the best device performance, which greatly increases the occurrence of secondary phases and concentrations of point defects and donor-acceptor defect complexes.[11–17] While intrinsic point defects in certain amount are beneficial for the doping and recombination characteristic of the kesterite phase, large concentrations of defect complexes can in turn lead to limiting minority charge carrier lifetimes and enhance recombination processes.[2] Defects can also have an effect on the net band gap variations and cause localized band gap or electrostatic potential fluctuations,[18] which can lead to change in the bulk diffusivity and indirectly affect the optoelectronic properties.

Moreover, a convergence of kesterite-based device efficiencies towards the record of 12% has been observed in recent years, with no significant breakthrough. While there is a consensus that poor bulk properties in the absorber layer are the most likely limiting factor for devices, there is no an actual agreement on the origin of this issue. It is hoped that advances in defect and device engineering will enable better understanding of the intrinsic limitations of this material and help to reach higher solar cell efficiencies.

In this context, thorough assessment of the absorber layer in terms of crystalline quality, defect qualification and quantification, homogeneity, as well as the identification of secondary phases is of foremost importance. It has already been demonstrated that Raman spectroscopy is one of the most suitable techniques for determining the crystalline structure and quality of semiconductor thin films, as the intensity, shape and position of Raman peaks are strongly influenced by the presence of defects in the material, either in the form of structural inhomogeneities or secondary phases.[19–23] In the case of kesterite materials, clear variations in the Raman spectral features with composition,[15,16] annealing temperature,[24,25] doping,[26–29] and excitation wavelengths[30,31] have been reported in the literature.

However, in many cases, the origin of these changes is not completely explained. In order to avoid misapprehensions and inaccuracies in the analysis of the Raman measurements and to make this technique useful for future kesterite development, a better understanding of the vibrational properties of these promising semiconductor compounds is required.

In many cases, Raman measurements of the kesterite phase are done under green excitation (514.5 or 532.0 nm), which is one of the most common in Raman spectroscopy systems. However, in recent years, it was proven that utilization of additional wavelengths in the Raman analysis is very beneficial and often gives complementary information. This is especially true for the secondary phase identification, where application of the resonant Raman effect plays an invaluable role. Tuning the incident photon energy of the Raman measurements with the energy band gap of the secondary phase, leads to a strong enhancement of the secondary phase Raman modes, which in turn provides their more straightforward detection. For example, blue excitation wavelength allows very accurate detection of ZnSe, which is the most expected secondary phase in Zn rich and Cu poor CZTSe layers.[32] On the other hand, red and near infrared (NIR) excitation conditions are adequate for copper selenides, tin selenides and copper-tin selenides assessment.[33] Even though, detection of these phases is of most importance due to their impact on the optoelectronic properties of the solar cells, it still remains a challenge by standard techniques such as x-ray diffraction (XRD), where an overlap of the main reflections of both CZTSe and its secondary phases is observed. Moreover, the intrinsic bulk analysis of XRD technique usually impedes the detection of such secondary phases which tend to segregate at the absorber layer surface in very low concentrations.

Furthermore, regardless of secondary phase presence, application of different excitation energies in Raman spectroscopy studies can also induce changes in the intensities of the intrinsic Raman peaks of kesterites. As mentioned previously, tuning of the incident photon energy with the electronic band transition energy, leads to resonance effects, with a strong increase in the intensity of peaks associated with that particular transition.[34] As a result, certain Raman peaks which could not be observed under non-resonant excitations, could be strongly enhanced in the spectra measured under resonant conditions. This kind of appearance of “new” peaks in the spectra, can often lead to false interpretations. Thus, it is important to first understand the behaviour of all Raman peaks of non-contaminated and pristine kesterite material under different excitation conditions, before applying this technique for further studies.

In that framework, the first part of this work is focused on a detailed investigation of the Raman mode behaviour and identification of all Raman active modes for polycrystalline CZTSe thin films using nine different excitation wavelengths (325.0, 442.0, 457.9, 514.5, 532.1, 632.8, 784.6, 830.0 and 1064.0 nm). In principle, near resonance Raman effects are expected to be the main factors influencing variations in the Raman spectra of CZTSe with the changes in the excitation wavelength. This study focuses on two Raman resonant conditions: (1) resonance under NIR (1.17 eV ~ 1064 nm) excitation (linked to the CZTSe bandgap) and (2) resonance under ultra-violet (UV) (3.81 eV ~ 325 nm) excitation (linked to the direct Γ_3 and/or E_{1B} transition in the CZTSe electronic structure). The experimental results compare well with the vibrational frequencies that have been computed by first-principles calculations based on density functional theory (DFT). Calculations of the phonon density of states, as well as the simulation of the Raman spectra, have allowed a better understanding of the nature of experimentally observed vibrational modes.

The second part of this work is centred on a systematic study of defect clusters and point defects in CZTSe material and their assessment by Raman spectroscopy using UV resonant conditions. As already mentioned, using resonant Raman conditions in kesterite materials are particularly interesting due to the enhanced sensitivity of the technique to modifications of material properties. However, under NIR excitation conditions, a strong photoluminescence (PL) background coupled with a low Raman efficiency of CZTSe, compromise the application of bandgap related resonant conditions. Alternatively, the use of UV excitation enables higher sensitivity than under standard measuring conditions without the typical photoluminescence contribution. Up to date, UV Raman spectroscopy was mostly used for identification of ZnS-related secondary phases in both CZTS and CZTSSe materials,[5,35–40] however, there is no current bibliography which reports in-depth study of CZTSe materials using this excitation wavelength. UV Raman spectroscopy is also interesting for its low penetration depth into the material (< 10 nm), which makes UV Raman measurements very surface sensitive. This work reports a thorough investigation of the CZTSe material properties under UV excitation, allowing an enhanced sensitivity of the Raman features to structural-compositional changes without the characteristic photoluminescence background of bandgap related resonant conditions. Additionally, intensities of particular peaks are linked with defect clusters/point defects concentrations.

Experimental details

Materials preparation

Pure selenide kesterite absorbers (CZTSe) with stoichiometric and lateral composition gradients were grown by a two-stage process. Firstly, metallic stacks of Sn/Cu/Zn were deposited by direct current (DC) magnetron sputtering onto Mo (800 nm) coated soda lime glass substrates as described in detail in Ref. [[41]]. These precursor stacks (5x5 cm^2) are further reactively annealed in a graphite box containing elemental Se and Sn powders (100 mg Se and 5 mg Sn) inside of a conventional three zone tube furnace under argon atmosphere. A two-step temperature profile is used for annealing. First a selenization at 400 ºC for 30 minutes under argon flow (keeping the pressure at 1.5 mbar) is carried out, followed by a second shorter annealing at 550 ºC for 15 minutes under constant 1000 mbar argon pressure to improve crystallinity. Cooling is allowed naturally to room temperature which normally takes about two hours. After the absorber growth, a surface etching procedure was performed for ZnSe and SnSe phase removal, using $KMnO_4$ and $(NH_4)_2S$ solutions respectively.[42,43]

Certain samples were then made into solar cell devices by adding a CdS buffer layer (50 nm), which was deposited by chemical bath deposition (CBD). Immediately after CdS growth, the solar cells were completed by DC-pulsed sputtering deposition of i-ZnO (50 nm) and In_2O_3-SnO_2 (ITO, 350 nm) as transparent conductive window layer (Alliance CT100). Afterwards, for the optoelectronic characterization, 3×3 mm^2 cells were mechanically scribed using a manual microdiamond scriber MR200 OEG. Neither antireflective coating nor metallic grids were used for the optoelectronic characterization of the devices. Absorber composition was evaluated by XRF analysis (Fisherscope XDV).

A total of four types of samples were produced and used in this work:

1) a reference CZTSe film with an optimal copper-poor and zinc-rich composition, typical for high efficiency CZTSe devices as reported in ref. [4], which was used for Raman spectroscopy characterization with different excitation wavelengths;

2) a chemically etched CZTSe film with a lateral gradient composition, which was used for studying the influence of composition and defect cluster concentration on the UV Raman spectra;

3) a similar CZTSe film as in case (2), with a smaller range of lateral gradient compositions around the high efficiency area, which was fabricated into 3x3 mm^2 solar cells. This sample was used for correlating Raman features with device optoelectronic properties;

4) An 11.0% efficiency device with optimized synthesis process with removed window and buffer layers.

Table 1 summarizes the process and compositional properties of the different samples used in this work.

Table 1. Composition and details of CZTSe samples used in this work

Sample	Composition	[Cu]/([Sn]+[Zn])	[Zn]/[Sn]	Type and quantity
1	homogeneous	0.95	1.12	1 etched absorber
2	high lateral gradient	0.55-0.90	1.1-2.0	100 etched absorbers
3	lower lateral gradient	0.76-1.02	1.02-1.44	225 3x3 mm^2 complete devices
4	homogeneous	0.78	1.26	11% device efficiency with metallic grid and antireflective coating

Characterization

Raman scattering measurements were performed using different systems. Measurements performed under 325, 442, 633 and 830 nm excitation wavelengths were made with an optical probe developed at IREC and specifically optimized for each wavelength. The probe was coupled with an optical fibre to a FHR640 Horiba Jobin Yvon spectrometer. A macro-spot size of about 70 μm was used for acquiring a representative area of the absorber. T64000 Horiba Jobin-Yvon spectrometer was used for measurements with 457.9 and 514.5 nm wavelengths, in back- scattering configuration, in macro mode with a spot of around 100 μm in diameter. Finally, measurements under 532, 785 and 1064 nm excitation wavelengths were obtained via a LabRam HR800-UV setup in a back-scattering configuration. Excitation and light collection were made through an Olympus metallographic microscope in this system, with a laser spot size of the order of 1–2 μm (depending on the excitation wavelength). To avoid effects in the spectra related to potential microscopic inhomogeneities, the spot was moved over an area of 30x30 μm^2 utilizing the DuoScan™ accessory. For all measurements, a reference monocrystalline silicon sample has been used for calibration of the Raman frequency,

imposing the main peak position at 520 cm^{-1}. Power density of all excitation sources was kept low enough (< kW/cm^2) in order to avoid thermal effects.

Theoretical calculations

The calculation of the crystalline structure of CZTSe has been optimised with respect to both internal forces and external pressure using Density Functional Theory (DFT), with the exchange-correlation functional of Perdew, Burke, and Ernzerhof revised for solids (PBEsol). Total energy and forces were calculated using the VASP code, an 880 eV plane-wave cutoff, and a Γ-centred *k*-point mesh with 4 × 4 × 4 subdivisions for the primitive unit cell. The projector augmented-wave method including scalar-relativistic effects was employed. Beginning with a CZTSe structure and doing all-electron calculations with the same functional, it was found to be necessary to include in the calculations the semi-core Cu 3*p* states (and not the Sn 4*d* states) in order to converge the total energy and stress tensor. Even if none of these states are involved in the chemical bonding, they can influence indirectly the valence electronic structure and hence atomic forces. Internal structural parameters were converged to within 10^{-7} eV or until the magnitude of the forces on the ions was less than 10^{-2} eV/Å. The Castep package was used for lattice dynamics, including structure generation and post-processing using the direct (supercell) approach. Force constants were computed from a 2 × 2 × 2 supercell expansion, with the *k*-point sampling reduced accordingly. During post-processing, phonon frequencies were computed on a 16 × 16 × 16 Γ-centred *q*-point mesh, which was sufficient for convergence of the phonon DOS with the chosen supercell size.

Results and discussion

Multiwavelength CZTSe vibrational study

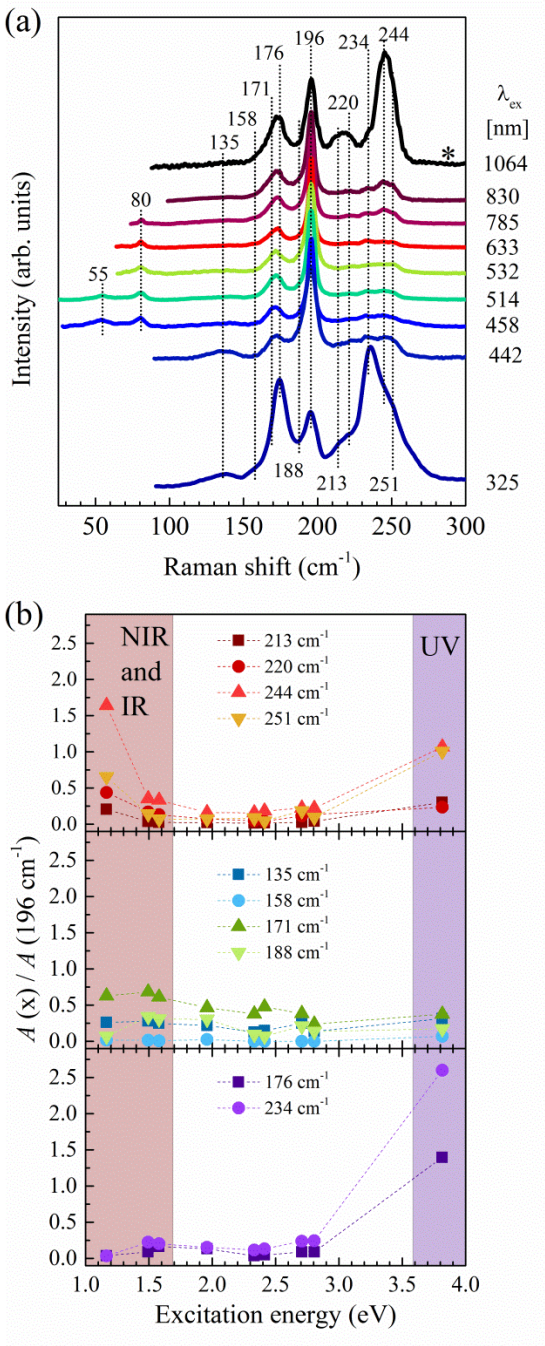

Figure 1. (a) Raman spectra of polycrystalline CZTSe reference thin film measured with different excitation wavelengths. (*) indicates that the PL background has been substracted. (b) Area ratio of the various Raman CZTSe peaks in reference to the peak at 196 cm^{-1}, as a function of laser excitation energy. For convenience, all modes are divided into three groups according to the behaviour of their relative area under the different resonant conditions. Colored bands on the figure mark excitation wavelenghts under which resonant Raman effect is observed in the case of CZTSe.

The ground-state crystal structure of CZTSe is kesterite with a space group $I\bar{4}$. According to the group theory analysis,[44,45] in Mulliken notation, the total irreducible representation for the zone centre (Γ point) phonon modes is given as:

$$\Gamma = (B \oplus E) \oplus (3A \oplus 6B \oplus 6E).$$

Here, the *A* and *B* modes are non-degenerate, while the *E* modes are double degenerate. Based on the selection rules for this crystal symmetry, one *B* mode and one *E* mode are acoustic, 3*A*, 6*B* and 6*E* are Raman active, while only the 6*B* and 6*E* modes are IR active. According to the irreducible representation, a total of 15 modes are predicted to be observed in the Raman spectra. On the other hand, the removal of degeneracy between the longitudinal optical (LO) and transverse optical (TO) phonons (LO-TO splitting) near the Brillouin zone centre is expected for the *B* and *E* modes, due to the dipole created by displacements of charges in the long-wave longitudinal phonons.[46] This is resulting in 28 Raman peaks ideally expected to be observed experimentally for this type of material.

However, this is usually not the case. The difference between the theoretically predicted and experimentally observed number of modes in the case of CZTSe, can be explained by several facts: (1) The acoustic modes can become Raman active, due to the crystal imperfections and defects, which create acoustic phonon confinement, resulting in localized vibrational modes which can be observed in low frequency part of the Raman spectra.[47] (2) The LO-TO splitting would not impose significant changes in the mode frequencies, as based on the DFT calculations for kesterite,[48,49] only several of the *B* and *E* symmetry modes might possess relatively large LO-TO splitting of 10 to 20 cm^{-1} (in the frequency range above 200 cm^{-1}), while other modes are only weakly polar and exhibit smaller splitting. This will result in each LO-TO pair usually generating only one broad peak.. Recent polarization Raman measurements on monocrystalline CZTSe samples performed by Guc et al.,[50] have experimentally observed and identified 15 Raman peaks.

Figure 1(a) presents the experimental Raman spectra of reference CZTSe thin film measured under different excitation wavelengths. Simultaneous fittings of spectra with Lorentzian curves using the same methodology as for CZTS reported in Dimitrievska et al.,[30] allowed obtaining a very good deconvolution of the CZTSe Raman spectra. A total of 13 peaks have been identified and attributed to the vibrational modes expected in this case.

Table 2 lists the Raman frequencies off all peaks obtained from the deconvolution, the excitation condition under which the peak is most intense, and symmetry assignment from the comparison with pervious experimental works and theoretical calculations. Comparative analysis based on the intensity and the peak positions has shown a good agreement between the experimental and theoretical results, as well as with the previously reported data.

Table 2. Frequency (in cm^{-1}) of peaks from Lorentzian fitting of Raman spectra measured with different excitation wavelengths and proposed mode symmetry assignment compared with theoretical predictions and reported experimental data from literature.

Literature				This work		
ν_{theory} (cm^{-1})[51]	ν_{theory} (cm^{-1})[48]	Symmetry assignment[50]	ν_{exp} (cm^{-1})[50]	ν_{exp} (cm^{-1})	λ^{*} (nm)	Type of area dependence**
				55.0 (A***)	514	--
74.4 + 74.6 85.4 + 85.6 81.0 + 81.0	73.6 + 73.8 82.8 + 82.9 83.0 + 82.9	B^1(TO+LO) B^2(TO+LO) E^2(TO+LO)	77 82	80.2	514	--
159.0 + 159.1	141.1 + 141.8	E^3(TO+LO)	138	135.2	442	2
171.5 + 171.8	156.7 + 157.3	B^3(TO+LO)	157	158.0		2
181 183.6	162.8 166.5	A^1 A^2	170 174	171.0	514/532	2
202.5 + 211.3	175.3 + 178.7	B^4(TO+LO)	178	175.5	325	3
205.4 + 208.8	179.0 + 180.5	E^4(TO+LO)	189	188.0		2
196.2	186.3	A^3	196	195.6	514/532	(Ref)
217.4	199.8	E^5(TO)	224	212.6	1064	1
219.9	202.8	E^5(LO)	231	220.1	1064	1
223.4	204.2	B^5(TO)	235	233.8	325	3
226	205.4	B^5(LO)	239			--
231.1	227.1	B^6(TO)	245	243.9	1064	1
236	228.8	B^6(LO)	250	250.9	830	1

* Excitation wavelength where a maximum intensity of the specific peak was found.

** Type of the dependence of the area of peak from the excitation wavelength, corresponding to one of the panel in the Fig. 1 (b). Type 1 represents Raman peaks which experience significant increase in intensity under both NIR and UV excitations. Type 2 represents Raman peaks which are not prone to increase in intensity under either NIR or UV excitations. And type 3 represents Raman peaks which intensity is significantly enhanced only under UV excitation conditions.

*** Peak assigned to the acoustic mode

Looking at the dependence of the peak area (A(peak X)) normalized to the area of the CZTSe main peak(A(peak at 196 cm^{-1})) with the excitation energy (Figure 1(b)), it is easily noticeable, that all peaks experience drastic changes under UV, NIR and IR excitations. Raman spectra measured with 532 nm excitation are characterized with an intense *A* mode at 196 cm^{-1} and several weaker contributions attributed to second *A* and polar *B* and *E* modes. Increase and decrease in excitation energy induces negligible spectrum variations until reaching 442 nm (2.81 eV) and 830 nm (1.49 eV) excitations, when a slight increase in intensities of peaks at 176 and 244 cm^{-1} is observed. With further changes in the excitation energy, the intensity of these peaks almost doubles, as seen for 325 nm (3.81 eV) and 1064 nm (1.16 eV) nm excitations. The Raman spectra measured with 1064 nm excitation is dominated by the peak at 244 cm^{-1} attributed to the *B*(TO) mode, while spectra measured with 325 nm excitation is dominated by two peaks at 176 and 234 cm^{-1} associated with *E*/*B*(LO) modes.

This kind of peak intensity behaviour can be explained by the Raman resonance effects. Considering the theoretical calculations on the electronic band structure for CZTSe, which have estimated the energies of Γ1 point (band gap energy) and Γ2 point as 0.90 eV and 3.12 eV, respectively, it is expected that near resonance Raman effect will be observed for excitation wavelengths of 1064, 830.0, 785.0, and 442.0 nm, with corresponding energies of 1.16, 1.49, 1.58, and 2.81eV. The most pronounced effects of the resonance conditions are perceived for *E* and *B* symmetry Raman modes, which are IR active and experience LO-TO splitting due to their polar character.[52] It is interesting to remark that these modes are observed as very weak contributions in standard Raman scattering conditions (514-532 nm), where the spectra are dominated by the two main *A* symmetry modes at 171 and 196 cm^{-1}, which are not IR active. On the other hand, the resonance effect observed with 325 nm (3.81 eV) excitation, is explained by inter-band transitions E(Γ3) and/or E_{1B} which are estimated to be in the range from 3.73 to 3.92 eV by ellipsometry measurements.[53]

The selective enhancement in intensity of specific Raman modes under resonance conditions means that resonance Raman spectroscopy is especially useful for studying changes in the material which will contribute to the changes in the atomic vibrations, such as compositional fluctuations and defects. First principle DFT calculations were performed in order to identify atomic vibrations involved in each Raman mode in the CZTSe material. This is achieved by calculating the phonon density of states (PDOS) for each element, as well as total PDOS. The PDOS are then used for the simulation of the Raman spectra, which showed a very good agreement with the experimental measurements, as can be seen in Figure 2.

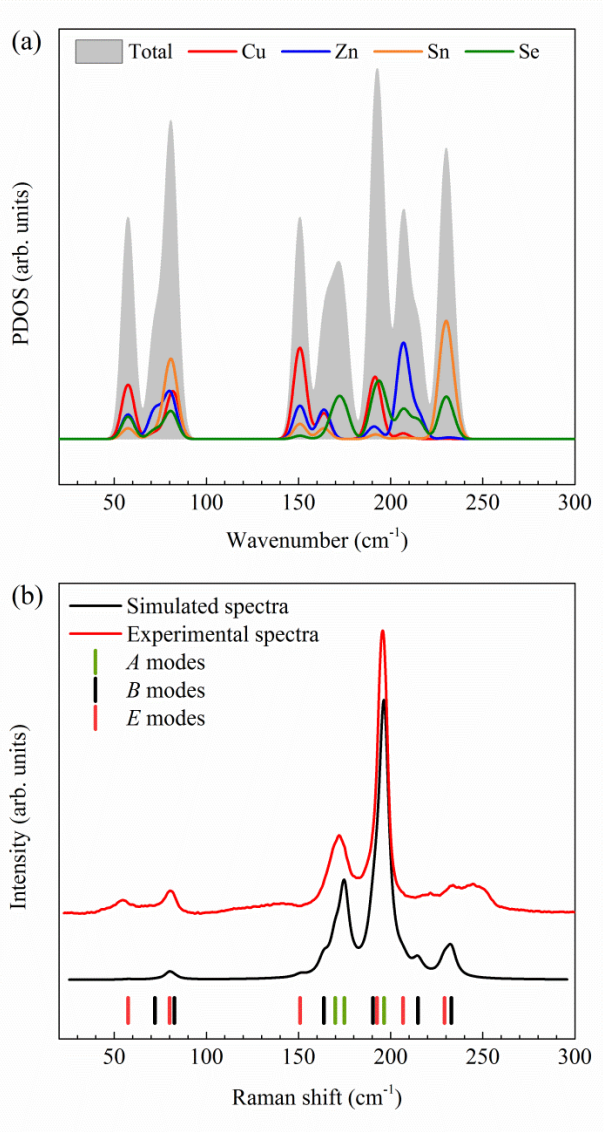

Figure 2. (a) Calculated elemental and total phonon density of states (PDOS) and (b) simulated and experimental Raman spectra of kesterite-structured CZTSe. The simulated Raman spectra have been broadened with the calculated 300 K phonon lifetimes. The experimental Raman spectra were measured on reference CZTSe thin film with 532 nm excitation. Vertical lines note the positions of the theoretical Raman modes. Note that LO-TO splitting is not included in the calculated spectra.

Based on the PDOS results and in agreement with previous reports,[49,54–56] the non-polar *A* modes are mostly originated from vibrations of Se atoms. On the other hand, the polar modes, besides the contributions from Se vibrations, also include vibrations from the cations. In particular, the lower frequency modes (in the range from 150 to 200 cm^{-1}) are arising due to vibrations involving Cu and Zn, while the high frequency modes (in the range from 200 to 250 cm^{-1}) are derived from the vibrations involving Sn and Zn. Having in mind that the intensity of the Raman modes is directly proportional to the density of states, which in turn depend on the concentration of the ions, it can be concluded that the changes in the intensity of the Raman modes can be correlated with changes in the

elemental concentration of the material, and thus with the concentration of the created compositional defects. This is why Raman spectroscopy is a very suitable technique for investigating the nature and concentration of defects in materials.

Using resonance Raman conditions can enhance detection of certain types of defects, as the intensity of specific Raman modes is increased, meaning that the sensitivity to changes in the intensity is additionally elevated. However, not all resonant conditions are suitable for these kinds of studies. For example, Raman measurements under 1064 nm excitation wavelength, even though considered resonant, are relatively compromised in the case of CZTSe due to the strong photoluminescence effect. An example of CZTSe Raman spectra measured under these conditions is shown in Figure S1 in the Supporting Information. While the photoluminescence (PL) signal can be removed during the data analysis, it is still time consuming, taking into account the need to have a suitable signal/noise ratio allowing detection of small changes in the Raman spectra. In some cases this PL contribution can be misleading, which makes this excitation wavelength unsuitable for defect studies in the CZTSe case.

On the other hand, non-band gap resonant Raman conditions, such as with 325 nm wavelength are much more suitable. As seen in Figure 1, Raman measurements with this excitation especially enhance modes at 176 cm^{-1} and 234 cm^{-1}, which involve Cu and Zn, and Sn and Zn vibrations, respectively, and can be used as a reference for defects related to these elements, as explained in the next section.

Influence of the compositional defects on the vibrational properties of CZTSe

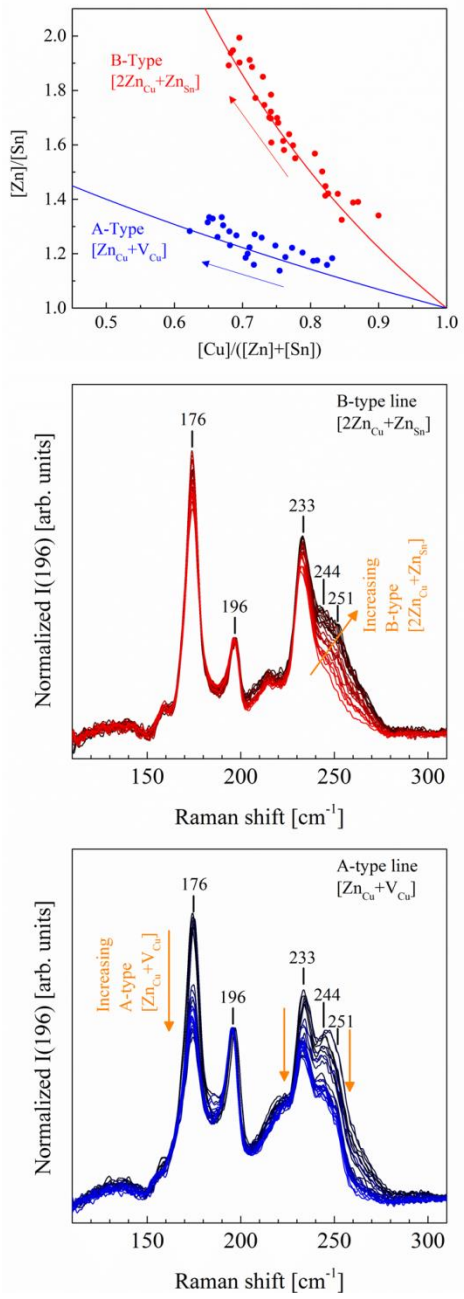

Figure 3. (Top) Compositional mappings of the samples. Blue and red lines correspond to sample compositions leading to a monotonous change in the density of type A ([Zn_{Cu} + V_{Cu}]) and type B ([$2Zn_{Cu}$ + Zn_{Su}]) defect clusters, respectively. Blue and red dots correspond to the selected set of samples with different A and B-type defect clusters concentration, respectively. Arrows indicate in which way the defect cluster concentrations increase. (Middle and Bottom) Raman spectra of samples with composition close to A-type (Middle) and B-type (Bottom) defect cluster lines measured with 325 nm excitation wavelength. For clarity, all spectra are normalized to the 196 cm^{-1} peak intensity.

It is assumed that samples synthesized under the exactly defined compositional conditions for formation of certain types of defects will contain only those defects. This is because the concentrations of the defect clusters that arise in a given sample, depend on the availabilities (i.e., the chemical potentials) of the different elements during synthesis. For example, if excess Zn is available during synthesis, then some of this may be incorporated in the CZTSe phase, via the formation of B-type defect complexes [Zn_{Sn}+2Zn_{Cu}]. Under certain compositional conditions, only certain defect complexes are formed, due to the formation energy of that defect complex being the lowest when compared to others. This essentially means that there are compositional conditions which will favor the formation of only B-type of defects. Theoretically, under these conditions no other defect complexes should be formed, due to their formation energy being higher.

Combinatorial methods; whereby thin films are deposited with smooth gradients in composition over their surface in one or more directions are an excellent way to provide these specific compositional conditions under which specific type of defects could be formed. In order to investigate the influence of defects on the vibrational properties of the CZTSe compound, thin film with lateral compositional gradients have been prepared as explained in the Experimental Section (Sample 2), with a composition range of Cu/(Zn+Sn) from 0.55 to 0.90 and Zn/Sn from 1.10 to 2.00. This film is then used for the fabrication of a high number of samples (100), each one with different absorber composition (Figure S2 in the Supporting Information). The distinctive composition of enables formation of the different types and concentrations of defects within each sample.

Compositional mapping of these samples is shown in Figure 3(a), along with the A and B type defect lines, corresponding to a monotonous variation of the concentration of [V_{Cu}+Zn_{Cu}] (A type) and [Zn_{Sn}+2Zn_{Cu}] (B type) charge compensated point defect clusters, respectively.[15–17,54,57,58]

The corresponding Raman spectra measured under 325 nm excitation are shown in Figure 3(b) for the samples following the A-type compositional line, and Figure 3(c) for the samples following the B-type compositional line. Obvious changes in the areas of the Raman peaks at 176 and 234 cm^{-1} and of the 250 cm^{-1} spectral region (related to the contribution of both 244 and 251 cm^{-1} Raman peaks), that are attributed to *E*/*B* modes, can be observed with the changes in the composition. These changes are much more pronounced under this resonant condition, rather than with standard measurements performed with 532 nm excitation. A comparison between the Raman spectra measured with 325 and 532 nm excitation, for CZTSe samples with different compositions is presented in Figure S3 in the Supporting Information.

Figure 4 presents the evolution of the relative area of the Raman peak at 176 cm^{-1} and the Raman band at 250 cm^{-1} as a function of the sample composition, for composition changes leading to changes in the content of A-type and B-type cluster defects. The relative area of the peaks is calculated as A(peak X)/[A(peak X)+A(196 cm^{-1})], where A(peak X) is the area of the Raman peak at the position X and A(196 cm^{-1}) is the area of the main *A* symmetry peak at 196 cm^{-1}.

The area of the Raman peak located at 176 cm^{-1} looks unaffected by the B-type defect cluster concentration ([2Zn_{Cu}+Zn_{Sn}]) (Figure 4(a)). This indicates that this peak is independent from both Zn_{Cu} and Zn_{Sn} point defect concentrations. On the other side, increasing the A-type defect cluster concentration leads to a decrease in the area of this peak (Figure 4(c)). As the A-type defect line is related to [Zn_{Cu}+V_{Cu}] defect cluster, and having in mind the previous conclusion, it is reasonable to

assume that the area of the Raman peak at 176 cm^{-1} is reduced when the concentration of copper vacancies, V_{Cu}, increases, while the concomitant increase of Zn_{Cu} defects seems to have a residual influence on the area of the peak. This is in agreement with the previously reported results, where changes in the area of this peak measured under 532 nm excitation were also correlated to the Cu substitutional defects.[16,54] Note that the peak at 234 cm^{-1} exhibits a similar behaviour to that of the peak at 176 cm^{-1} (correlation between the relative area of these two peaks is presented in Figure S4 in the Supporting Information).

The origin of the changes in the area of the Raman band centred at 250 cm^{-1}, which corresponds to the contributing peaks at 244 and 251 cm^{-1}, is more complex. In this case the area of the band increases when the content of the B-type ($[2Zn_{Cu}+Zn_{Sn}]$) defect clusters increases (Figure 4(b)), while it decreases when the content of the A-type ($[Zn_{Cu}+V_{Cu}]$) defect clusters increases (Figure 4(d)). This suggests that the Zn_{Cu} point defect, which is present in both kinds of defect clusters, is not related to these changes. These results indicate that the band at 250 cm^{-1} is sensitive to the content of both Zn_{Sn} and V_{Cu} point defects. However, the overlapping of the 244 and 251 cm^{-1} peaks in this band does not allow to assign the change of the area of each of the peaks with a specific type of defects.

These results are in good agreement with the theoretical calculations and the PDOS, where it is observed that the Raman mode at 176 cm^{-1} is mostly related to vibrations of the Cu atoms. On the other hand, the origin of the changes for the Raman band at 250 cm^{-1} is more difficult to interpret due to the discrepancy between the experimental and theoretical results. This discrepancy is mostly due to not including LO-TO splitting in the calculations of the spectra. However, based on the previous reposrts,[48] the inclusion of LO-TO splitting would additionally increase the frequencies of the Raman modes in the high frequency region. Thus, it might be reasonable to assume, that the Raman band at 250 cm^{-1} is mostly related to vibrations of the Sn atoms with a possible contribution from vibrations of Zn atoms, as this corresponds to the tail of the PDOS, which would be in a agreement with the experimental results.

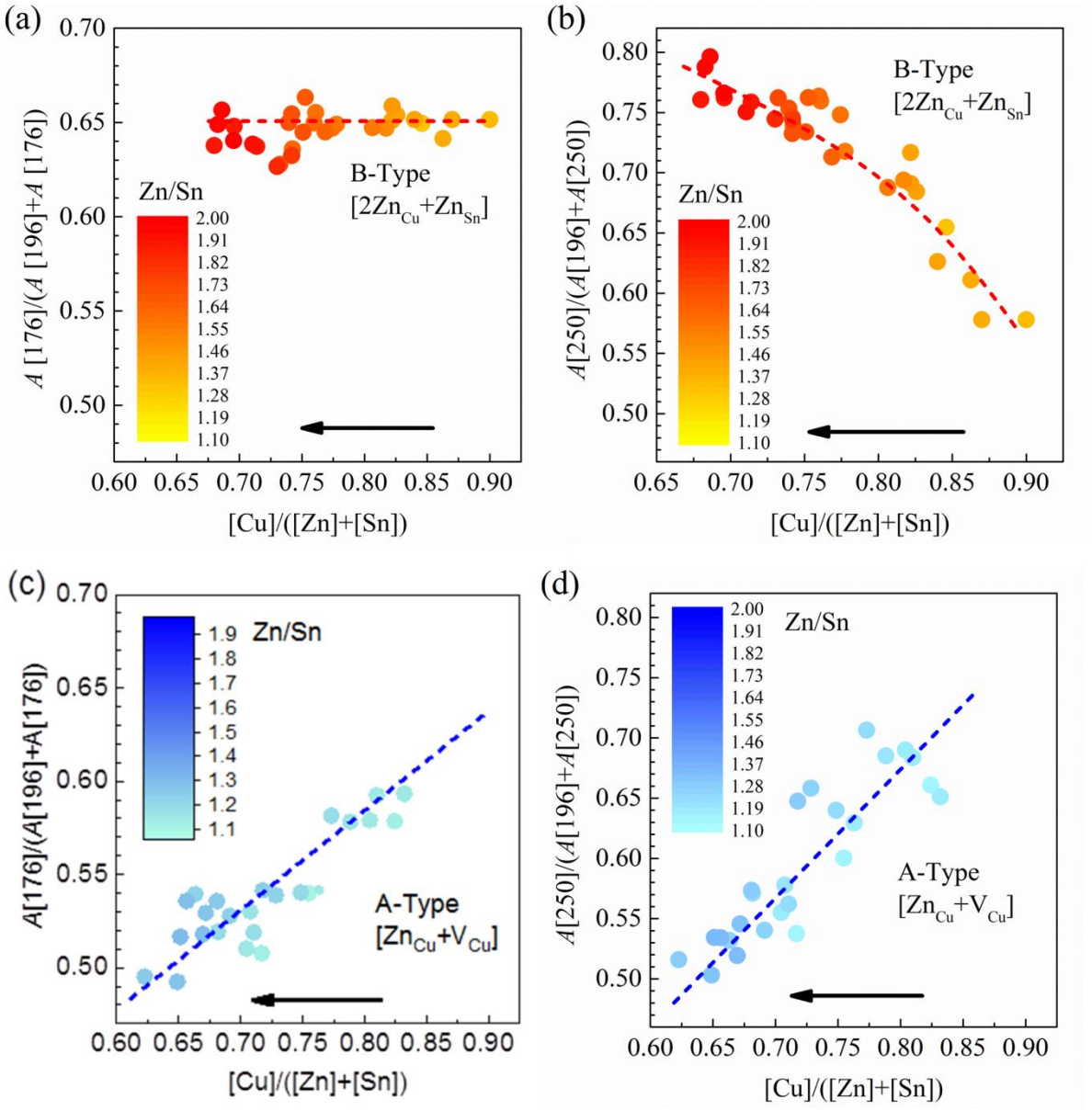

Figure 4. Relative area of Raman modes located at 176 cm^{-1} ((a) and (c)) and close to 250 cm^{-1} region ((b) and (d)) as a function of composition. Defect cluster type are also provided as support: graphs (a) and (b) involve samples with composition close to the B-type defect line, while graphs (c) and (d) correspond to samples with composition close to the A-type defect line. The direction of the arrow indicates the increase in the defect cluster concentration.

Influence of the compositional defects on optoelectronic properties of the CZTSe solar cells

In order to obtain a deeper understanding of the absorber composition and defect related effects on the optoelectronic properties, a CZTSe sample with a laterally graded composition was prepared into solar cells as explained in the Experimental section (sample 3). Mappings of the optoelectronic properties with around 200 points showing device efficiency, open-circuit voltage (V_{OC}), short-circuit current (J_{sc}) and fill factor (*FF*) are presented in Figure S5 in the Supporting Information.

After the optoelectronic characterization, the sample was etched with HCl solution in order to perform UV Raman spectroscopy assessment of the absorber surface without any interference from the window and buffer layers.

As in the previous case, the relative areas of the Raman modes at 176 cm^{-1} and in the region at 250 cm^{-1} have been used to assess the impact of specific defect clusters on the optoelectronic properties. Figure 5 presents the correlation between the relative Raman area, which is related to the concentration of the different defects, and the V_{oc}, J_{sc}, *FF* and efficiency of the final devices.

Figures 5 (left) shows the existence of an optimum value of the relative area of the 176 cm^{-1} Raman peak at about 0.58 that leads to a maximum value of the V_{oc} , FF and efficiency, while the optimum value leading to a maximum J_{sc} is slightly shifted to 0.60. As has been previously discussed, changes in the relative area of the 176 cm^{-1} peak are mainly related to changes in the concentration of the shallow acceptor V_{Cu}, which is one of the defects that determines the concentration of the majority carriers (holes) in the CZTSe absorber. The presence of a maximum in the efficiency supposes an existence of an optimum content of the V_{Cu} defect: Above this optimum value (corresponding to a relative area of the 176 cm^{-1} Raman peak below the optimal value close to 0.58) the high content of defects leads to a reduction of the carrier mobility and to an increase of the recombination rate, degrading the performance of the device. On the other hand, below this optimum value (corresponding to a relative area of the 176 cm^{-1} Raman peak above the optimal value close to 0.58), the density of carriers is too low, which leads to an increase of the space charge zone. These experimental data prove the high sensitivity of the proposed methodology for the assessment of the V_{Cu} optimal defect content in the absorber layers. On the other hand, the shift of the optimum value corresponding to the maximum J_{sc} in relation to that corresponding to the maximum V_{oc} agrees with the differences that have already been reported on the optimal absorber composition region leading to devices with maximum V_{oc} and J_{sc} values, respectively [17].

Figures 5 (left) shows a similar behaviour with the existence of an optimal value of the relative intensity of the 250 cm^{-1} Raman band at about 0.62 leading to devices with a maximum value of Jsc, FF and efficiency. In this case, changes in the intensity of the band are related to changes in the content of both V_{Cu} and Zn_{Sn} defects. However, the overlapping between the Raman peaks contributing to this bad complicates the interpretation of this behaviour.

The behaviour observed for both the relative intensity of the 176 cm^{-1} Raman peak and of the 250 cm^{-1} Raman band reflect the importance of controlling CZTSe defect cluster concentrations for the achievement of high device efficiencies. This methodology offers a screening of absorbers, which will give the possibility of choosing the most suitable ones, which in addition to optimization of the other layers of solar cell will achieve will give the best performing device.

In order to test this behaviour, a reference CZTSe absorber with compositional [Cu]/([Zn]+[Sn]) and [Zn]/[Sn] ratios of about 0.78 and 1.26, respectively, has been analysed. This absorber composition corresponds to devices that show an efficiency of 11 % (after deposition of a metallic grid and an antireflective coating). Deconvolution of the corresponding absorber Raman spectra measured under 325 nm excitation (Figure 6 (b)) has given relative areas of the Raman peak at 176 cm^{-1} and of the Raman band at 250 cm^{-1} of 0.57 and 0.65, respectively. These values are in good agreement with the optimal values shown in Figure 5 for the achievement of devices with improved performance. These

preliminary assessments of CZTSe defects by Raman spectroscopy may serve as a guideline for further development of the technology.

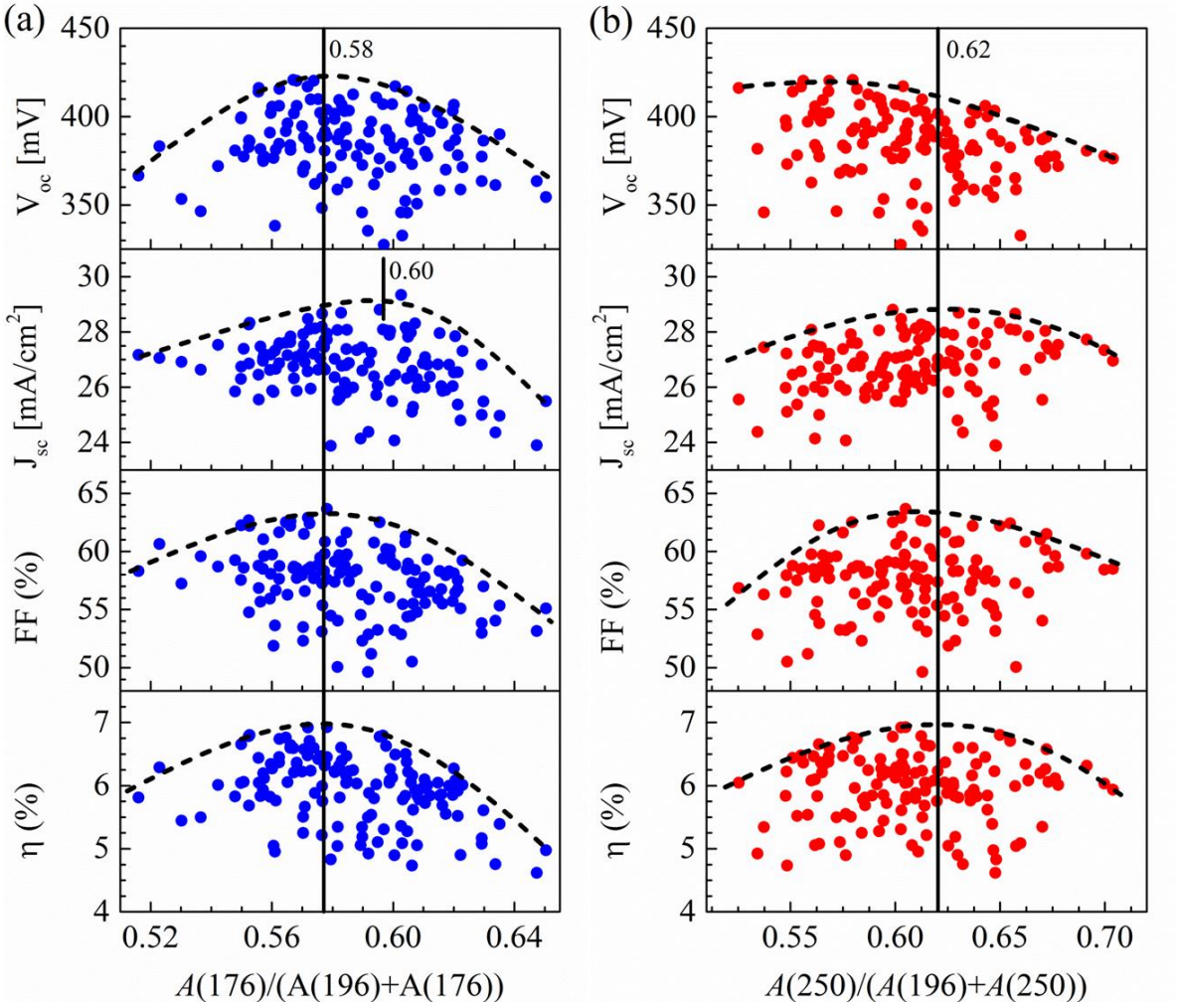

Figure 5. Correlation of optoelectronic properties with the relative area of the Raman modes located at the (a) 175 cm^{-1} and (b) 250 cm^{-1} spectral regions. The dashed lines indicate the upper limit for each otpeoelectronic parameter, and the vertical solid lines indicate the area ratios corresponding aproxialy the maxima of the V_{oc}, J_{sc}, FF, and Eff.

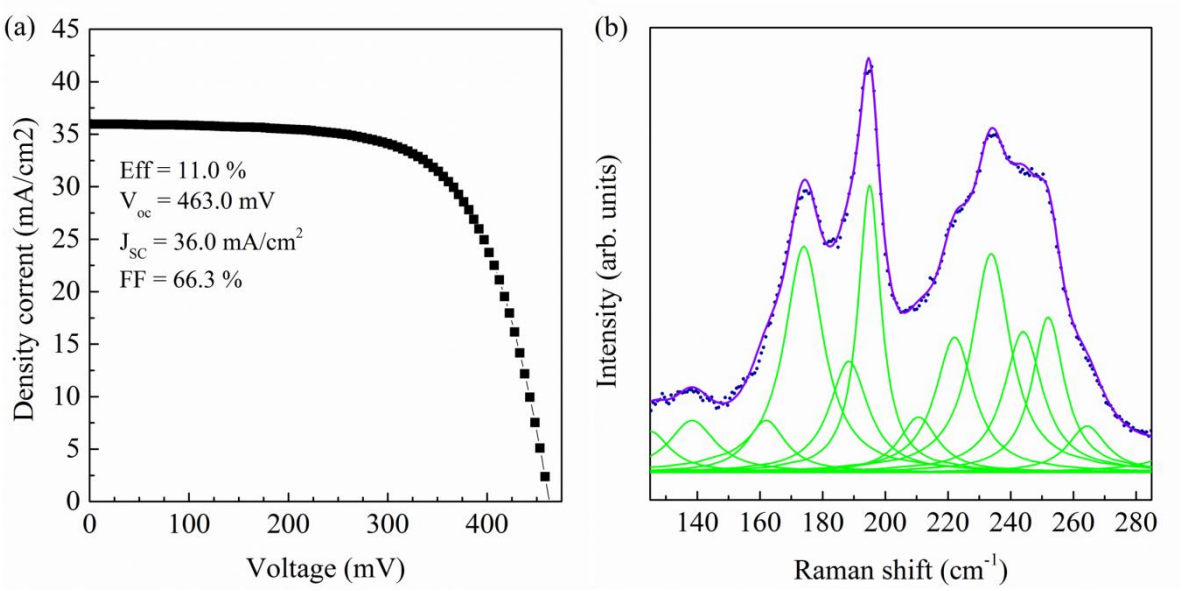

Figure 6. (a) IV curve of a high efficiency CZTSe based solar cell and (b) the corresponding Raman spectrum of its absorber layer under 325 nm excitation wavelength.

Conclusion

Polycrystalline kesterite $Cu_2ZnSnSe_4$ (CZTSe) semiconductors have drawn attention as promising absorber candidates for the next generation of thin film photovoltaics. However, the narrow tolerance to stoichiometry variations that favours the formation of secondary phases and cluster defects is a challenging drawback that restrains the device performances. In this context Raman spectroscopy has demonstrated to be a powerful tool for the characterization of CZTSe, allowing the assessment of the relevant parameters such as structure, crystal quality and secondary phases.

This work is focused on a detailed investigation of the Raman mode behaviour and identification of all Raman active modes for polycrystalline CZTSe thin films using nine different excitation wavelengths (325.0, 442.0, 457.9, 514.5, 532.1, 632.8, 784.6, 830.0 and 1064.0 nm). Near resonance Raman effects were observed to be the main factors influencing variations in the Raman spectra of CZTSe with the changes in the excitation wavelength. This study focuses on two Raman resonant conditions: (1) resonance under NIR (1.17 eV ~ 1064 nm) excitation (linked to the CZTSe bandgap) and (2) resonance under ultra-violet (UV) (3.81 eV ~ 325 nm) excitation (linked to the direct Γ_3 and/or E_{1B} transition in the CZTSe electronic structure). The experimental results compare well with the vibrational frequencies that have been computed by first-principles calculations based on DFT. Calculations of the phonon density of states, as well as the simulation of the Raman spectra, have allowed a better understanding of the experimentally observed vibrational modes.

Special focus is put on UV based Raman spectroscopy characterization, since a strong enhancement in the intensity of the spectral regions around 176 and 250 cm^{-1}, which are attributed to *E*/*B* modes, is observed. Combinatorial experiments on more than 200 samples with stoichiometry close to the compositions with which high efficiency devices are performed, in addition with DFT calculations.

The observed data allow to correlate the changes of the relative area of the 176 cm^{-1}Raman peak and of the 250 cm^{-1} Raman band a with changes in the concentration of V_{Cu} and Zn_{Sn} point defects, respectively. These have also been correlated to the optoelectronic properties of the devices, allowing identification of the optimal concentration of these point defects for the highest performance devices. The application of the presented methodology has been confirmed by performing the same Raman analysis on the CZTSe absorber with 11 % device efficiency. This work demonstrates that defect engineering in CZTSe is of the foremost importance for the improvement in the solar cell performance, and that UV-based Raman spectroscopy is an effective technique for the non-destructive assessment of defects in the kesterite materials. The possibility to apply micrometric methodologies for the Raman characterization opens the possibility for the indirect characterization of the composition and defect formation at microscale level and the evaluation of the potential limitation in the device performance of the micro homogeneity of the absorber.

Acknowledgements

This research was supported by the H2020 Programme under the projects STARCELL (H2020-NMBP-03-2016-720907) and INFINITE-CELL (H2020-MSCA-RISE-2017-777968), by the Spanish Ministry of Science, Innovation and Universities under the IGNITE (ENE2017-87671-C3-1-R) and WINCOST (ENE2016-80788-C5-1-R), and by the European Regional Development Funds (ERDF, FEDER Programa Competitivitat de Catalunya 2007–2013). Authors from IREC and the University of Barcelona belong to the SEMS (Solar Energy Materials and Systems) Consolidated Research Group of the "Generalitat de Catalunya" (Ref. 2017 SGR 862). SG thanks the Government of Spain for the FPI fellowship (BES-2014-068533). M.D. gratefully acknowledges support from the Hydrogen Materials - Advanced Research Consortium (HyMARC), established as part of the Energy Materials Network under the U.S. Department of Energy, Office of Energy Efficiency and Renewable Energy (DOE EERE), Fuel Cell Technologies Office, under Contract No. DE-AC36-08GO28308.

References

1 A. Walsh, S. Chen, S.-H. Wei and X.-G. Gong, *Adv. Energy Mater.*, 2012, **2**, 400–409.
2 S. K. Wallace, D. B. Mitzi and A. Walsh, *ACS Energy Lett.*, 2017, **2**, 776–779.
3 A. Polizzotti, I. L. Repins, R. Noufi, S.-H. Wei and D. B. Mitzi, *Energy Environ. Sci.*, 2013, **6**, 3171–3182.
4 W. Wang, M. T. Winkler, O. Gunawan, T. Gokmen, T. K. Todorov, Y. Zhu and D. B. Mitzi, *Adv. Energy Mater.*, 2014, **4**, 1301465.
5 K.-J. Yang, D.-H. Son, S.-J. Sung, J.-H. Sim, Y.-I. Kim, S.-N. Park, D.-H. Jeon, J. Kim, D.-K. Hwang, C.-W. Jeon, D. Nam, H. Cheong, J.-K. Kang and D.-H. Kim, *J. Mater. Chem. A*, 2016, **4**, 10151–10158.
6
7 S. Chen, X. G. Gong, A. Walsh and S.-H. Wei, *Appl. Phys. Lett.*, 2009, **94**, 041903.
8 H. Zhao and C. Persson, *Thin Solid Films*, 2011, **519**, 7508–7512.
9 W. Shockley and H. J. Queisser, *J. Appl. Phys.*, 1961, **32**, 510–519.
10 S. Rühle, *Sol. Energy*, 2016, **130**, 139–147.
11 S. Schorr, *Sol. Energy Mater. Sol. Cells*, 2011, **95**, 1482–1488.
12 D. B. Mitzi, O. Gunawan, T. K. Todorov, K. Wang and S. Guha, *Sol. Energy Mater. Sol. Cells*, 2011, **95**, 1421–1436.

13 A. Redinger, D. M. Berg, P. J. Dale and S. Siebentritt, *J. Am. Chem. Soc.*, 2011, **133**, 3320–3323.
14 S. Chen, X. G. Gong, A. Walsh and S.-H. Wei, *Appl. Phys. Lett.*, 2010, **96**, 021902.
15 A. Davydova, K. Rudisch and J. J. S. Scragg, *Chem. Mater.*, 2018, **30**, 4624–4638.
16 M. Dimitrievska, A. Fairbrother, E. Saucedo, A. Pérez-Rodríguez and V. Izquierdo-Roca, *Sol. Energy Mater. Sol. Cells*, 2016, **149**, 304–309.
17 A. Fairbrother, M. Dimitrievska, Y. Sánchez, V. Izquierdo-Roca, A. Pérez-Rodríguez and E. Saucedo, *J. Mater. Chem. A*, 2015, **3**, 9451–9455.
18 S. Chen, A. Walsh, X.-G. Gong and S.-H. Wei, *Adv. Mater.*, 2013, **25**, 1522–1539.
19 X. Fontané, V. Izquierdo-Roca, E. Saucedo, S. Schorr, V. O. Yukhymchuk, M. Y. Valakh, A. Pérez-Rodríguez and J. R. Morante, *J. Alloys Compd.*, 2012, **539**, 190–194.
20 X. Fontané, L. Calvo-Barrio, V. Izquierdo-Roca, E. Saucedo, A. Pérez-Rodriguez, J. R. Morante, D. M. Berg, P. J. Dale and S. Siebentritt, *Appl. Phys. Lett.*, 2011, **98**, 181905.
21 A.-J. Cheng, M. Manno, A. Khare, C. Leighton, S. A. Campbell and E. S. Aydil, *J. Vac. Sci. Technol. A*, 2011, **29**, 051203.
22 P. A. Fernandes, P. M. P. Salomé and A. F. da Cunha, *J. Alloys Compd.*, 2011, **509**, 7600–7606.
23 M. Dimitrievska, A. Fairbrother, A. Pérez-Rodríguez, E. Saucedo and V. Izquierdo-Roca, *Acta Mater.*, 2014, **70**, 272–280.
24 M. Dimitrievska, S. Giraldo, P. Pistor, E. Saucedo, A. Pérez-Rodríguez and V. Izquierdo-Roca, *Sol. Energy Mater. Sol. Cells*, 2016, **157**, 462–467.
25 G. Rey, A. Redinger, J. Sendler, T. P. Weiss, M. Thevenin, M. Guennou, B. E. Adib and S. Siebentritt, *Appl. Phys. Lett.*, 2014, **105**, 112106.
26 Z. Tong, C. Yan, Z. Su, F. Zeng, J. Yang, Y. Li, L. Jiang, Y. Lai and F. Liu, *Appl. Phys. Lett.*, 2014, **105**, 223903.
27 Z. Laghfour, S. Aazou, M. Taibi, G. Schmerber, A. Ulyashin, A. Dinia, A. Slaoui, M. Abd-Lefdil and Z. Sekkat, *Superlattices Microstruct.*, 2018, **120**, 747–752.
28 Z. Wang, N. Brodusch, R. Gauvin and G. P. Demopoulos, *Nano Energy*, 2018, **53**, 130–134.
29 M. Neuschitzer, J. Marquez, S. Giraldo, M. Dimitrievska, M. Placidi, I. Forbes, V. Izquierdo-Roca, A. Pérez-Rodriguez and E. Saucedo, *J. Phys. Chem. C*, 2016, **120**, 9661–9670.
30 M. Dimitrievska, A. Fairbrother, X. Fontané, T. Jawhari, V. Izquierdo-Roca, E. Saucedo and A. Pérez-Rodríguez, *Appl. Phys. Lett.*, 2014, **104**, 021901.
31 M. Dimitrievska, H. Xie, A. Fairbrother, X. Fontané, G. Gurieva, E. Saucedo, A. Pérez-Rodríguez, S. Schorr and V. Izquierdo-Roca, *Appl. Phys. Lett.*, 2014, **105**, 031913.
32 M. Dimitrievska, H. Xie, A. J. Jackson, X. Fontané, M. Espíndola-Rodríguez, E. Saucedo, A. Pérez-Rodríguez, A. Walsh and V. Izquierdo-Roca, *Phys. Chem. Chem. Phys.*, 2016, **18**, 7632–7640.
33 I. Becerril-Romero, L. Acebo, F. Oliva, V. Izquierdo-Roca, S. López-Marino, M. Espíndola-Rodríguez, M. Neuschitzer, Y. Sánchez, M. Placidi, A. Pérez-Rodríguez, E. Saucedo and P. Pistor, *Prog. Photovolt. Res. Appl.*, 2018, **26**, 55–68.
34 P. Y. Yu and M. Cardona, in *Fundamentals of Semiconductors: Physics and Materials Properties*, eds. P. Y. Yu and M. Cardona, Springer Berlin Heidelberg, Berlin, Heidelberg, 1996, pp. 107–158.
35 Z. Zhang, L. Yao, Y. Zhang, J. Ao, J. Bi, S. Gao, Q. Gao, M.-J. Jeng, G. Sun, Z. Zhou, Q. He and Y. Sun, *Adv. Sci.*, 2018, **5**, 1700645.
36 R. Sun, M. Zhao, D. Zhuang, Q. Gong, L. Guo, L. Ouyang and Y. Wei, *J. Alloys Compd.*, 2017, **695**, 3139–3145.
37 D. M. Berg, M. Arasimowicz, R. Djemour, L. Gütay, S. Siebentritt, S. Schorr, X. Fontané, V. Izquierdo-Roca, A. Pérez-Rodriguez and P. J. Dale, *Thin Solid Films*, 2014, **569**, 113–123.
38 J. Tao, J. Liu, L. Chen, H. Cao, X. Meng, Y. Zhang, C. Zhang, L. Sun, P. Yang and J. Chu, *Green Chem.*, 2016, **18**, 550–557.

39 J. Tao, L. Chen, H. Cao, C. Zhang, J. Liu, Y. Zhang, L. Huang, J. Jiang, P. Yang and J. Chu, *J. Mater. Chem. A*, 2016, **4**, 3798–3805.
40 K.-J. Yang, J.-H. Sim, D.-H. Son, D.-H. Kim, G. Y. Kim, W. Jo, S. Song, J. Kim, D. Nam, H. Cheong and J.-K. Kang, *Prog. Photovolt. Res. Appl.*, 2015, **23**, 1771–1784.
41 S. López-Marino, M. Placidi, A. Pérez-Tomás, J. Llobet, V. Izquierdo-Roca, X. Fontané, A. Fairbrother, M. Espíndola-Rodríguez, D. Sylla, A. Pérez-Rodríguez and E. Saucedo, *J. Mater. Chem. A*, 2013, **1**, 8338–8343.
42 S. López-Marino, Y. Sánchez, M. Placidi, A. Fairbrother, M. Espindola-Rodríguez, X. Fontané, V. Izquierdo-Roca, J. López-García, L. Calvo-Barrio, A. Pérez-Rodríguez and E. Saucedo, *Chem. – Eur. J.*, 2013, **19**, 14814–14822.
43 H. Xie, Y. Sánchez, S. López-Marino, M. Espíndola-Rodríguez, M. Neuschitzer, D. Sylla, A. Fairbrother, V. Izquierdo-Roca, A. Pérez-Rodríguez and E. Saucedo, *ACS Appl. Mater. Interfaces*, 2014, **6**, 12744–12751.
44 M. I. Aroyo, A. Kirov, C. Capillas, J. M. Perez-Mato and H. Wondratschek, *Acta Crystallogr. A*, 2006, **62**, 115–128.
45 M. I. Aroyo, J. M. Perez-Mato, C. Capillas, E. Kroumova, S. Ivantchev, G. Madariaga, A. Kirov and H. Wondratschek, *Z. Für Krist. - Cryst. Mater.*, 2009, **221**, 15–27.
46 C. H. Henry and J. J. Hopfield, *Phys. Rev. Lett.*, 1965, **15**, 964–966.
47 M. Fujii, Y. Kanzawa, S. Hayashi and K. Yamamoto, *Phys. Rev. B*, 1996, **54**, R8373–R8376.
48 A. Khare, B. Himmetoglu, M. Johnson, D. J. Norris, M. Cococcioni and E. S. Aydil, *J. Appl. Phys.*, 2012, **111**, 083707.
49 M. Dimitrievska, F. Boero, A. P. Litvinchuk, S. Delsante, G. Borzone, A. Perez-Rodriguez and V. Izquierdo-Roca, *Inorg. Chem.*, 2017, **56**, 3467–3474.
50 M. Guc, S. Levcenko, V. Izquierdo-Roca, X. Fontané, E. Arushanov and A. Pérez-Rodríguez, *J. Appl. Phys.*, 2013, **114**, 193514.
51 T. Gürel, C. Sevik and T. Çağın, *Phys. Rev. B*, 2011, **84**, 205201.
52 M. Susaki, N. Yamamoto, B. Prevot and C. Schwab, *Jpn. J. Appl. Phys.*, 1996, **35**, 1652.
53 M. León, S. Levcenko, R. Serna, I. V. Bodnar, A. Nateprov, M. Guc, G. Gurieva, N. Lopez, J. M. Merino, R. Caballero, S. Schorr, A. Perez-Rodriguez and E. Arushanov, *Appl. Phys. Lett.*, 2014, **105**, 061909.
54 M. Dimitrievska, A. Fairbrother, E. Saucedo, A. Pérez-Rodríguez and V. Izquierdo-Roca, *Appl. Phys. Lett.*, 2015, **106**, 073903.
55 N. B. Mortazavi Amiri and A. Postnikov, *Phys. Rev. B*, , DOI:10.1103/PhysRevB.82.205204.
56 J. M. Skelton, A. J. Jackson, M. Dimitrievska, S. K. Wallace and A. Walsh, *APL Mater.*, 2015, **3**, 041102.
57 A. Lafond, L. Choubrac, C. Guillot-Deudon, P. Deniard and S. Jobic, *Z. Für Anorg. Allg. Chem.*, 2012, **638**, 2571–2577.
58 L. E. Valle Rios, K. Neldner, G. Gurieva and S. Schorr, *J. Alloys Compd.*, 2016, **657**, 408–413.

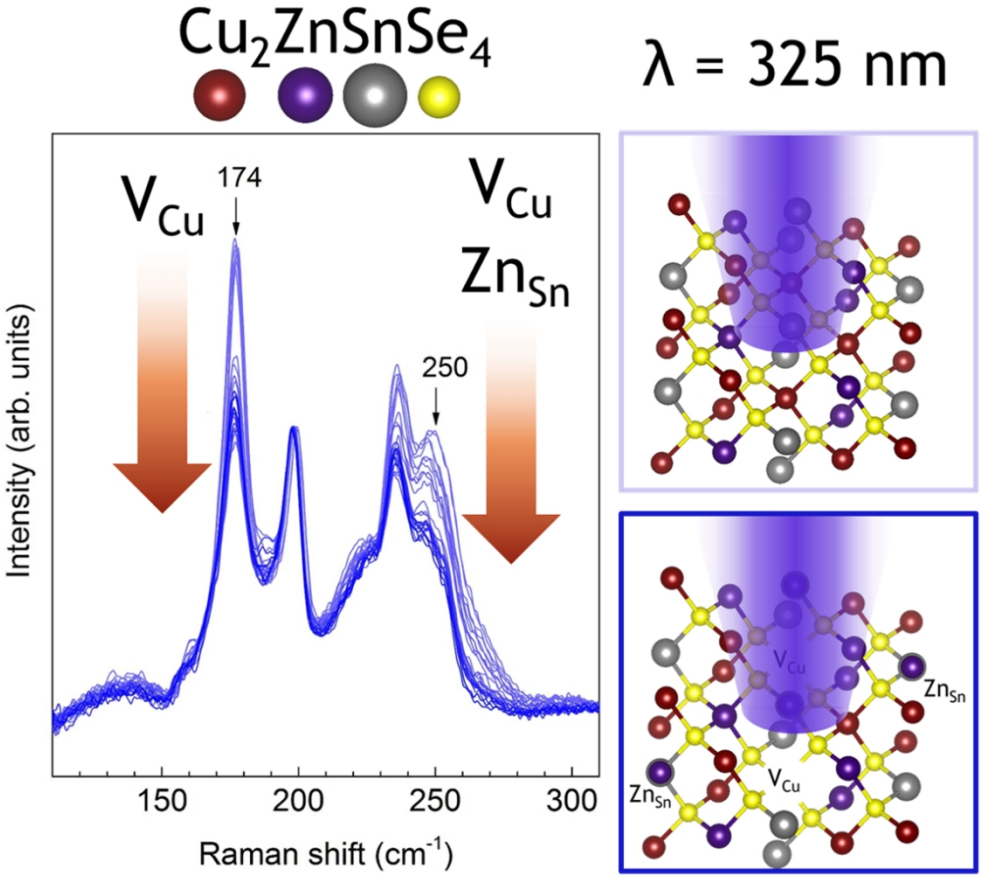

197x182mm (150 x 150 DPI)